

Article

Solid-State Synthesis of ZnO/ZnS Photocatalyst with Efficient Organic Pollutant Degradation Performance

Xuekun Jin ¹, Jianjun Chen ^{1,*}, Fengjuan Chen ^{2,3,*}, Haiming Duan ², Ziyu Wang ² and Junhua Li ¹¹ School of Environment, Tsinghua University, Beijing 100084, China² Key Laboratory of Solid State Physics and Devices Autonomous Region, School of Physics Science and Technology, Xinjiang University, Urumqi 830046, China³ Key Laboratory of Energy Materials Chemistry, Ministry of Education, Institute of Applied Chemistry, Xinjiang University, Urumqi 830046, China

* Correspondence: chenjianjun@tsinghua.edu.cn (J.C.); fjchen@xju.edu.cn (F.C.)

Abstract: To improve the separation efficiency of photogenerated carriers in ZnS, constructing a ZnS-based heterostructure with ZnO is assessed to be an efficient strategy, and a ZnO/ZnS photocatalyst was prepared by a solid-phase approach, and the structure and morphology were systematically studied. The ZnO/ZnS photocatalyst showed excellent photocatalytic properties on methyl orange, rhodamine B and tetracycline under UV light irradiation, indicating that the photocatalyst exhibited efficient broad-spectrum photocatalytic performance. Compared with ZnS, the degradation rates of ZnO/ZnS photocatalysts for methyl orange, rhodamine B and tetracycline under UV light increased from 21%, 9% and 32% to 96%, 94% and 93%, respectively, higher than the reported ZnO/ZnS composites synthesized by a novel wet chemical route, attributing to the improvement of light absorption ability and the effective separation of carriers. In addition, the influence of the sacrificial agent on the reaction system was investigated, and the synergistic mechanism of ZnO and ZnS in the catalytic process was analyzed according to the fluorescence spectra, photocurrent and first-principles calculation results, and a possible catalytic mechanism was put forward.



Citation: Jin, X.; Chen, J.; Chen, F.; Duan, H.; Wang, Z.; Li, J. Solid-State Synthesis of ZnO/ZnS Photocatalyst with Efficient Organic Pollutant Degradation Performance. *Catalysts* **2022**, *12*, 981. <https://doi.org/10.3390/catal12090981>

Academic Editor: Didier Robert

Received: 13 August 2022

Accepted: 30 August 2022

Published: 31 August 2022

Publisher's Note: MDPI stays neutral with regard to jurisdictional claims in published maps and institutional affiliations.



Copyright: © 2022 by the authors. Licensee MDPI, Basel, Switzerland. This article is an open access article distributed under the terms and conditions of the Creative Commons Attribution (CC BY) license (<https://creativecommons.org/licenses/by/4.0/>).

Keywords: ZnS; ZnO; pollutant; photocatalysis

1. Introduction

With the rapid development of industry, many refractory pollutants enter the water body, resulting in a series of environmental problems and a serious threat to human health [1–3]. Photocatalytic technology has become an effective way to solve the above problems due to its advantages of having a high efficiency, a simple process, and providing environmental protection. The core of this technology is high-efficiency photocatalysts [4–7]. Among them, ZnS has high electron reduction ability and hole oxidation ability, and is non-toxic and harmless, cheap and easy to obtain, and stable in performance, exhibiting broad prospects in dealing with refractory pollutants [8–11]. However, the recombination rate of photogenerated carriers is fast, and the photon quantum efficiency is low. Therefore, it is of great significance to develop efficient photocatalysts and apply them to remove refractory pollutants.

In view of the fast recombination rate of photogenerated carriers in ZnS, various approaches were adopted to enhance the photocatalytic activity, such as doping noble metals, recombining with semiconductors, etc. [12–15]. Among them, ZnO with high photocatalytic activity and suitable energy band is well matched with ZnS to improve the separation efficiency of photogenerated carriers, thereby improving the photocatalytic activity [16–18]. For example, Wang et al. prepared Pt/ZnS-ZnO nanosheets by a wet chemical method. It was found that the photocatalyst exhibited excellent photocatalytic performance due to the formation of a new path for electron transfer from ZnS to ZnO, and the activity was three times higher than that of ZnS nanowire arrays [19]. Therefore, constructing ZnO/ZnS

photocatalysts can improve the efficient separation of photogenerated carriers, which is an effective way to obtain high-efficiency photocatalysts.

It is well known that the performance of a photocatalyst is closely related to its structure and morphology, which mainly depends on the preparation approach. So far, although many methods were carried out to fabricate ZnS composites, such as electrospray method, thermal deposition method, thermal reduction method, etc. [20–24], the above methods have the disadvantages of high reaction temperature, complicated process and high energy consumption. Therefore, it is important to synthesize ZnO/ZnS photocatalysts by a simple and green method. The low-heat solid-phase chemical method refers to the reaction between solid substances at a low temperature. It has the advantages of no solvent, low reaction temperature, simple synthetic process, and environmental protection [25–28]. In recent years, our group has synthesized a series of nanofunctional materials with excellent catalytic performance by the simple low-heat solid-state chemical method [29–33]. However, the research on the synthesis of ZnO/ZnS photocatalysts by this method has not been reported yet.

In this work, ZnO/ZnS photocatalysts were prepared by a low-heat solid-state chemical method, and a series of characterizations were carried out on the phase, morphology, composition, and optical properties. The photocatalytic activity of the ZnO/ZnS photocatalyst was studied using Methylene Orange (MO), Rhodamine B (RhB) and tetracycline to simulate dye wastewater. The results showed that ZnO/ZnS photocatalyst exhibited excellent photocatalytic performance. At the same time, the influence of the composition and structure of the ZnO/ZnS photocatalyst on the photocatalytic performance were explored, and the influence of the sacrificial agent on the reaction system was investigated. The synergistic performance of ZnO and ZnS in the catalytic process was elucidated by photocurrent and fluorescence spectroscopy, and the photocatalytic mechanism was discussed in combination with theoretical calculations, which provided a theoretical basis for the design of efficient and broad-spectrum photocatalysts.

2. Results

2.1. Composition, Structure and Optical Properties

The phase composition of the sample was studied by XRD technique and is shown in Figure 1. Many obvious characteristic diffraction peaks were observed in ZnO, ZnS and ZnO/ZnS photocatalysts, which were consistent with the results reported in the literature. As the molar ratio of ZnO to ZnS in the ZnO/ZnS photocatalyst gradually changed from 9:1 to 5:95, the characteristic peaks of the ZnO/ZnS photocatalyst were also different, indicating that the molar ratio played an effect on the phase composition. When the molar ratio of ZnS to ZnO was 1:9, ZOS-0.1 showed obvious diffraction peaks at 32.1° , 34.6° and 36.5° , which were consistent with the diffraction peaks of ZnO (JCPDS 36-1451) [34]. When the molar ratio of ZnO to ZnS was 5:5, the composite ZOS-0.5 has obvious diffraction peaks at 28.7° , 47.6° and 56.5° , which was consistent with the diffraction peaks of ZnS (JPCDS 05-0566) [35]. In addition, as the ZnS content increased, the diffraction peaks of the composites also gradually enhanced, indicating that ZnS covers the shallow surface of ZnO, which had a certain influence on the crystal structure.

Figure 2 shows the TEM images of ZnS, ZnO and ZnO/ZnS photocatalyst ZOS-0.9. As can be seen from Figure 2a, ZnS was a random nanoparticle with a diameter of about 50 nm, and there was a certain degree of agglomeration. ZnO mainly existed in the form of nanorods with lengths between 30 and 80 nm and diameters between 5 and 30 nm (Figure 2b). ZOS-0.9 was mainly in the form of particles, and the particle size was reduced to about 5 nm (Figure 2c). Moreover, some ZnO nanorods can be seen in ZOS-0.9, which was beneficial to the synergistic effect of enhancing the separation efficiency of photogenerated carriers. The structure of the ZnO/ZnS photocatalyst was further investigated by the HRTEM technique (Figure 2d). The lattice spacing of 0.32 nm corresponded to the (111) facet of cubic phase ZnS, and the crystal plane spacing of 0.24 nm were ascribed to the (101) facet of hexagonal phase ZnO. Furthermore, there was an interface between the crystal

facets, which can improve the separation and transport rate of photogenerated charges, thereby enhancing the photocatalytic efficiency [36,37]. The SAED image (inset of Figure 2d) showed that ZOS-0.9 exhibited a polycrystalline diffraction ring, indicating that it had an obvious polycrystalline structure, which was also consistent with the XRD results.

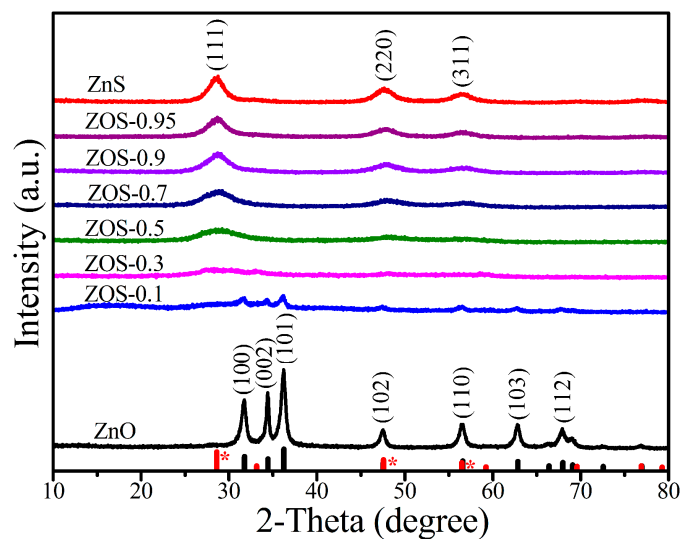


Figure 1. XRD patterns of ZnO, ZnS, and ZnO/ZnS photocatalysts.

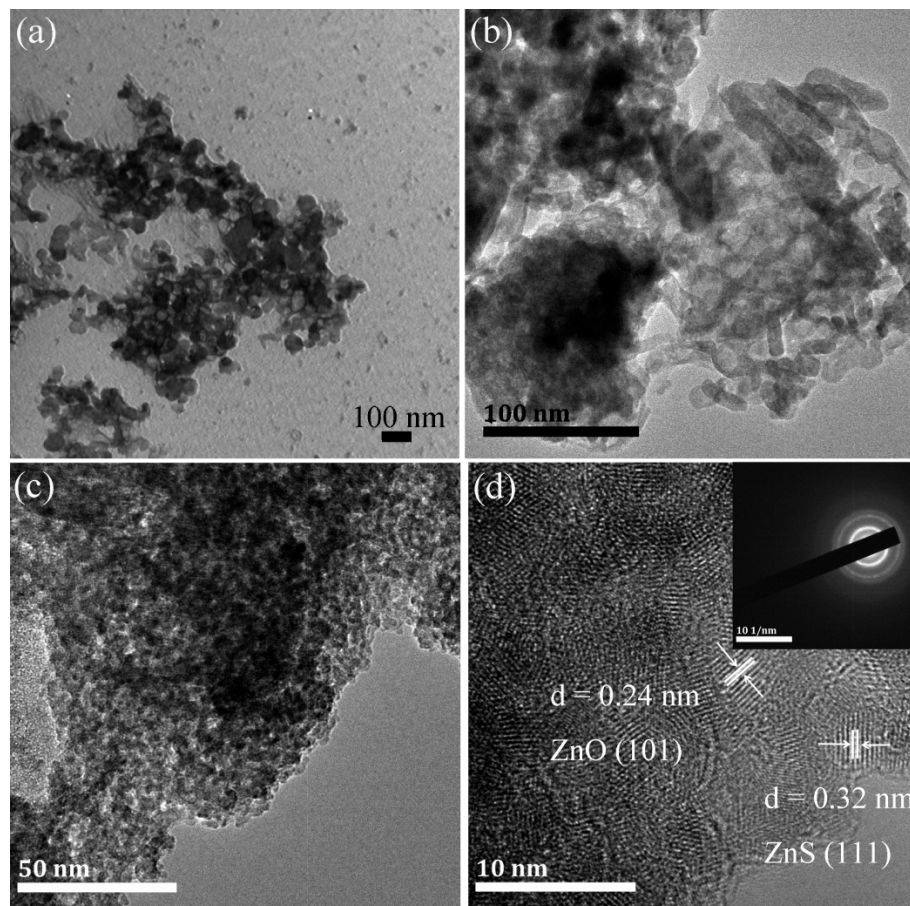


Figure 2. TEM images of ZnS (a), ZnO (b), and ZnO/ZnS photocatalyst ZOS-0.9 (c); HRTEM image (d), and SAED patterns (inset of d) of ZOS-0.9.

Figure 3a,b were TEM images of ZOS-0.7 at different magnifications. It can be seen that a large number of ZnS nanoparticles and some ZnO nanorods can be seen (Figure 3b), indicating the existence of ZnO and ZnS in the composites. Meanwhile, the structure of the ZnO/ZnS photocatalyst was further studied by HRTEM (Figure 3c). The lattice spacing of 0.32 nm was ascribed to the (111) facet of cubic ZnS, and the lattice spacing of 0.25 nm was assigned to the (101) crystal plane of hexagonal ZnO, and there was a clear interface between ZnO and ZnS, which was helpful to the synergistic effect of improving the separation efficiency of photogenerated carriers [36]. The SAED image (Figure 3d) showed that ZOS-0.7 exhibited polycrystalline diffraction rings, indicating an obvious polycrystalline structure, which was in agreement with the XRD results.

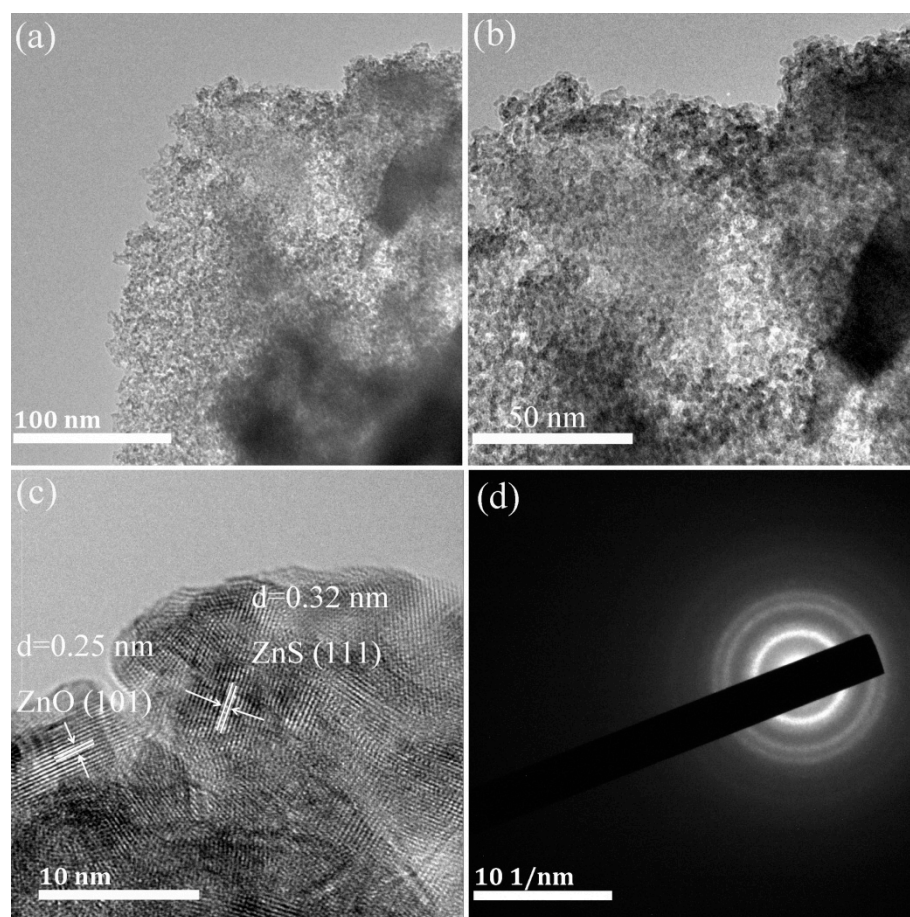


Figure 3. TEM images (a,b), the corresponding HRTEM image (c), and SAED patterns (d) of ZOS-0.7.

The compositions of ZnO, ZnS and ZOS-0.9 were studied by XPS technique and are shown in Figure 4. The full XPS spectra results indicated that ZnO contained Zn, O, and C elements, ZnS contained Zn, S, O, and C elements, and ZOS-0.9 was composed of Zn, O, S, and C elements (Figure 4a). The C peak at 284.6 eV and the O peak at 531.6 eV are both derived from the contamination of the sample surface [38]. In Figure 4b, two characteristic peaks centered at 1022.0 eV and 1045.1 eV were derived from Zn 2p_{3/2} and Zn 2p_{1/2} orbitals, corresponding to Zn²⁺ in ZnO and ZnS [39]. The characteristic peaks at 161.8 eV and 162.7 eV in Figure 4c were assigned to the S 2p_{3/2} and S 2p_{1/2} orbitals of S²⁺ in ZnS, respectively, proving the existence of ZnS [40]. Compared with ZnS, the binding energies of S element in ZOS-0.9 were slightly shifted toward higher binding energies, which may be caused by the interaction between ZnO and ZnS. Furthermore, two characteristic peaks of O 1s orbital appeared at 530.1 eV and 531.6 eV in ZnO (Figure 4d), proving the existence of two chemical states of O element. Among them, the strong peak at 530.1 eV indicated the existence of lattice oxygen in ZnO, while the weak peak at 531.6 eV may have originated

from the adsorbed H₂O on the sample surface [41]. In comparison with ZnO, the O 1s peak of ZOS-0.9 was red-shifted to 531.8 eV, indicating an interaction existed between ZnO and ZnS. The above XRD, HRTEM and XPS results indicated that ZOS-0.9 was composed of ZnO and ZnS.

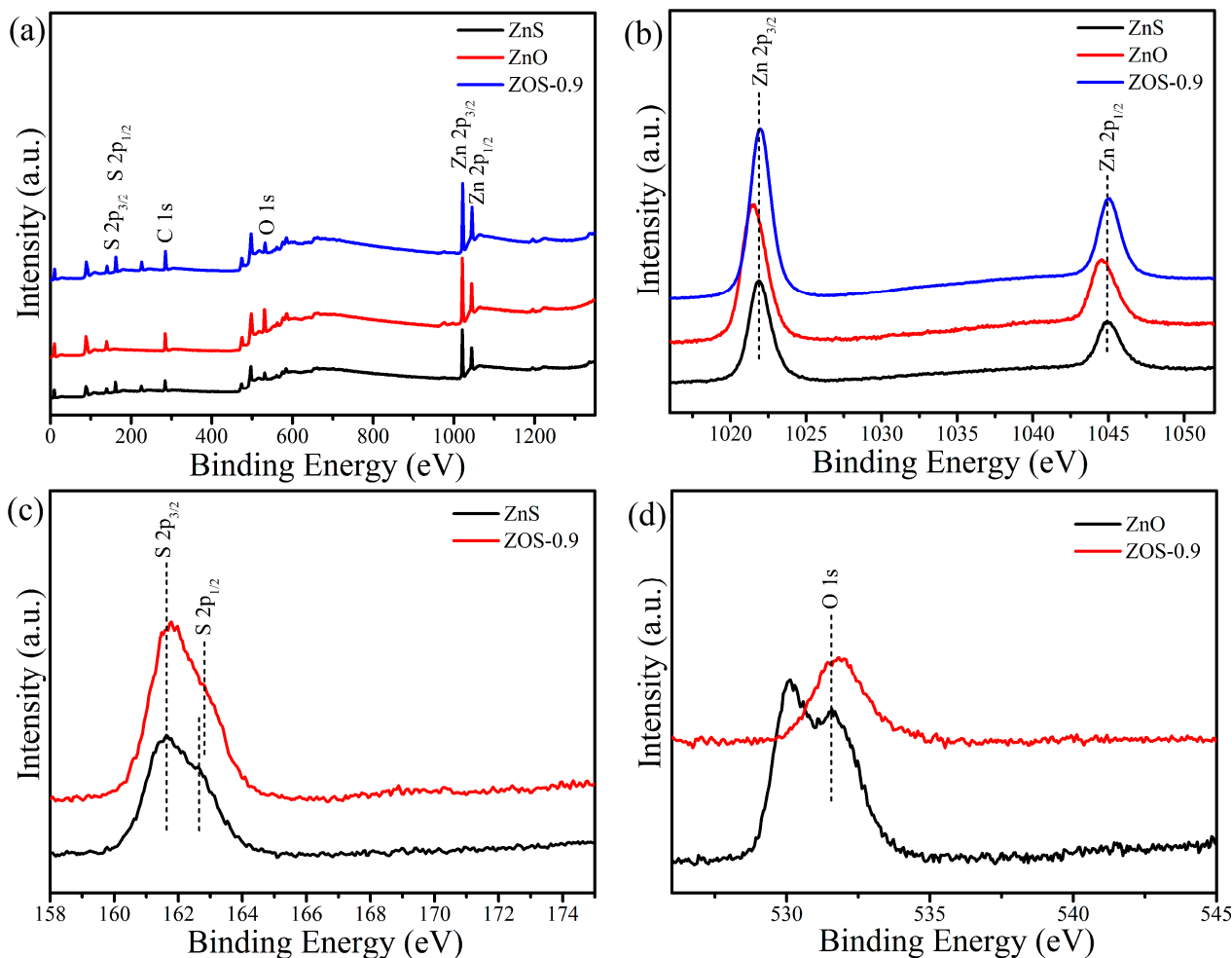


Figure 4. XPS spectra of ZnO, ZnS, and ZOS-0.9 (a) survey, (b) Zn 2p, (c) S 2p, (d) O 1s.

To study the optical properties of the samples, the UV-Vis diffuse reflectance properties of ZnO, ZnS and ZnO/ZnS photocatalysts were considered. In Figure 5a, the absorption edges of both ZnO and ZnS were around 380 nm. Compared with them, the absorption edge of ZnO/ZnS photocatalyst first shifted blue and then red with the increase in ZnS content. According to the formula $\alpha h\nu = A(h\nu - E_g)^{n/2}$, the forbidden band width of the semiconductor can be calculated. Since both ZnO and ZnS were direct bandgap semiconductors, n was taken as 1, and both sides were squared. Figure 5b was obtained by plotting $(\alpha h\nu)^2$ against the energy $h\nu$. A tangent was drawn, and the intersection of the tangent and the abscissa was the forbidden band width of the semiconductor [42]. It can be obtained that the forbidden band widths of ZnO, ZnS, ZOS-0.1, ZOS-0.3, ZOS-0.5, ZOS-0.7, ZOS-0.9 and ZOS-0.95 were 3.30 eV, 3.38 eV, 3.32 eV, 3.60 eV, 3.62 eV, 3.65 eV, 3.56 eV and 3.53 eV, respectively. Among them, ZOS-0.9 had a larger absorption edge and a smaller band gap. Therefore, it was more likely to be excited by light to generate carriers, and photocatalytic reactions were more likely to occur on the surface [43].

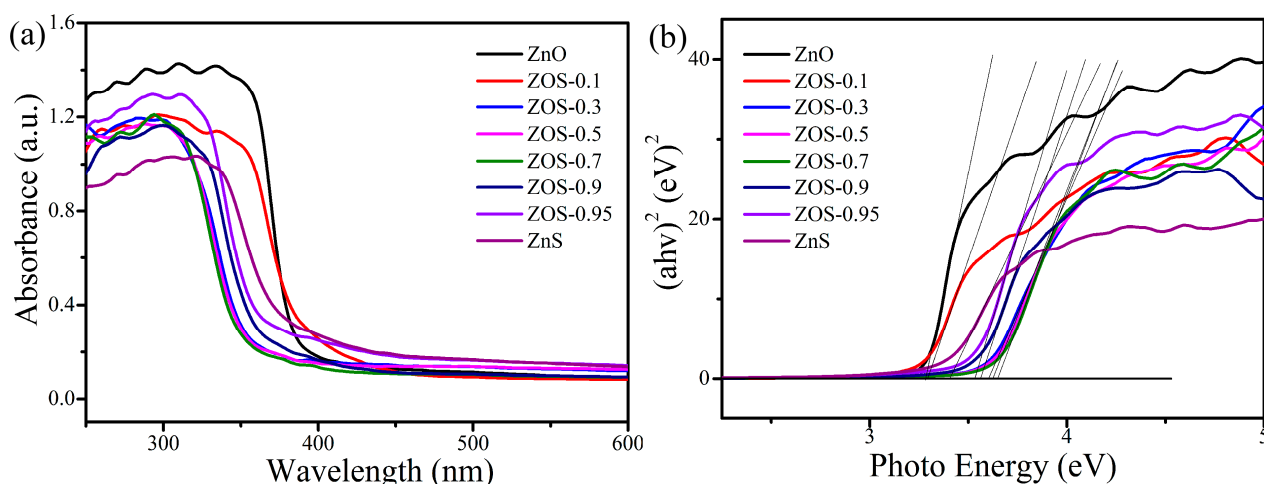


Figure 5. (a) UV-vis DRS, and (b) $(\alpha h\nu)^2$ versus $h\nu$ of ZnO, ZnS, and ZnO/ZnS photocatalysts.

2.2. Photocatalytic Performance

In order to explore the performance of the ZnO/ZnS photocatalyst, MO was used as a simulated dye to study the photocatalytic activity. Figure 6a shows the degradation of MO by ZnO, ZnS and ZnO/ZnS photocatalysts under UV light. The degradation rates of MO over ZnO and ZnS were 20% and 21% under 120 min illumination, respectively. When the ZnO/ZnS photocatalyst was added, the degradation rate of MO was significantly increased. Especially when the molar ratio of ZnS and ZnO was 9:1, ZOS-0.9 exhibited the highest degradation rate of MO, and the degradation rate reached 96% under 120 min illumination, which was superior to other reported chalcogenide composites [44]. It can be seen that the ZOS-0.9 can basically completely degrade MO molecules, indicating that the photocatalyst showed excellent degradation performance. It was mainly attributed to the introduction of ZnO, which facilitated the rapid separation of photogenerated carriers in photocatalysts, and was helpful to enhance to the ability of absorb light and store electrons, thereby improving the photocatalytic activity. To further investigate the reaction rate constant, a kinetic study was performed on the degradation data in Figure 6a [45]. In Figure 6b, the degradation rate constants of ZnO, ZnS and ZOS-0.9 for MO was 0.00175 min^{-1} , 0.00193 min^{-1} and 0.0202 min^{-1} , respectively. Thus, the degradation performance of ZOS-0.9 for MO was 12 times and 11 times to that of ZnO and ZnS, respectively, suggesting that the activity of ZnO/ZnS photocatalyst was significantly improved after introducing ZnO.

Meanwhile, the photocatalytic properties of ZnO/ZnS photocatalyst on the RhB under UV light irradiation were investigated. It can be seen that the composites also showed excellent photocatalytic activity for RhB (Figure 6c). After illumination for 120 min, the degradation rates of ZnO and ZnS were 46% and 9%, respectively, while 94% of RhB was degraded by ZOS-0.7, which was higher than that the reported [46], indicating that the ZnO/ZnS photocatalyst exhibited excellent photocatalytic activity in degrading RhB. From the kinetic curve in Figure 6d, the rate constants for degrading RhB by ZOS-0.7, ZnS and ZnO were 0.01536 min^{-1} , $0.000768 \text{ min}^{-1}$ and 0.00497 min^{-1} , respectively. Hence, the catalytic activity of ZOS-0.7 was 20 times and 3 times to that of ZnS and ZnO, respectively, indicating that the ZOS-0.7 exhibited excellent performance for the degradation of RhB.

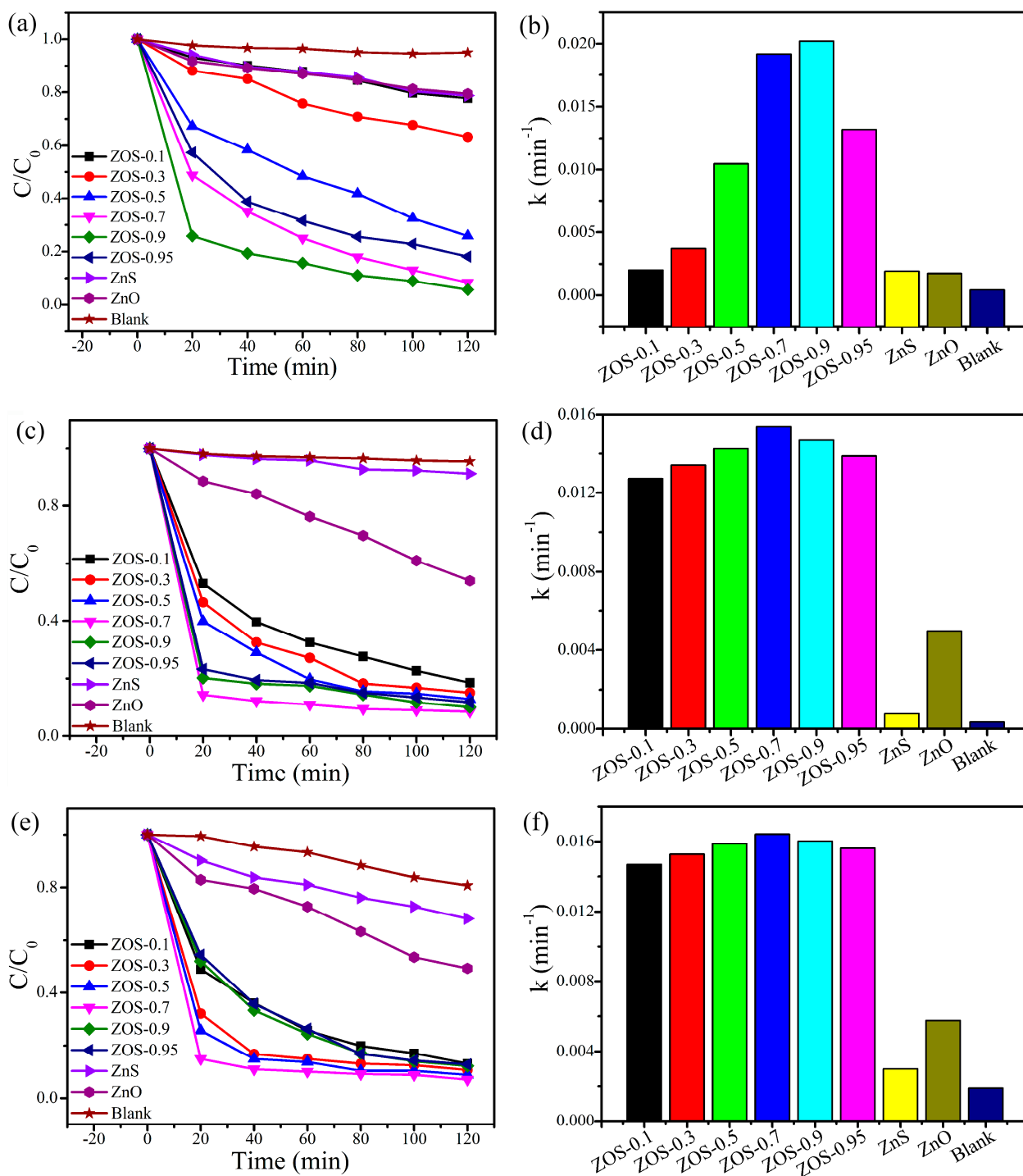


Figure 6. Photodegradation rates and kinetic curves under UV light for the degradation of MO (a,b), RhB (c,d), and tetracycline (e,f) over ZnO, ZnS, and ZnO/ZnS photocatalysts.

The photocatalytic performance of ZnO/ZnS photocatalyst for tetracycline was further studied. In Figure 6e, 32% of tetracycline was degraded by ZnS after 120 min of UV light irradiation, while the degradation rate of tetracycline by ZOS-0.7 reached 93%, which was higher than that the reported [47]. It can be seen that the photocatalyst ZOS-0.7 can basically completely degrade the tetracycline, indicating that the photocatalyst ZOS-0.7 showed excellent degradation performance for tetracycline. It can be attributed to the synergistic effect between ZnS and ZnO, and then promoting the rapid separation of photogenerated electrons and holes. Figure 6f showed the kinetic simulation results of degrading tetracy-

cline by ZnS, ZnO and ZnO/ZnS photocatalysts. The rate constants for the degradation of tetracycline by ZOS-0.7, ZnS and ZnO were 0.01642 min^{-1} and 0.00299 min^{-1} and 0.00576 min^{-1} , respectively. Compared with ZnS and ZnO, the catalytic activity of the ZOS-0.7 was 5.5 times and 2.9 times to that of the above, respectively, indicating that the photocatalyst exhibited excellent photocatalytic performance for tetracycline degradation.

Considering the importance of catalyst stability and reuse in practical applications, the stability of the ZOS-0.9 was investigated by cycling experiments and is shown in Figure S1. There was no significant decrease, and the degradation rate of MO can still reach 90% after being repeated 6 times, indicating that the ZnO/ZnS photocatalyst exhibited better stability.

2.3. Photocatalytic Mechanism

2.3.1. Theoretical Calculation

To study the ZnO/ZnS (ZOS) system, a 3×3 ZnS supercell was constructed with two S atoms replaced by O atoms and shown in Figure 7a. Band structures were calculated along the following high symmetry points in k-space: H $(-0.333, 0.666, 0.5)$, K $(-0.333, 0.666, 0)$, M $(0, 0.5, 0)$, Γ $(0, 0, 0)$, A $(0, 0, 0.5)$, L $(0, 0.5, 0.5)$.

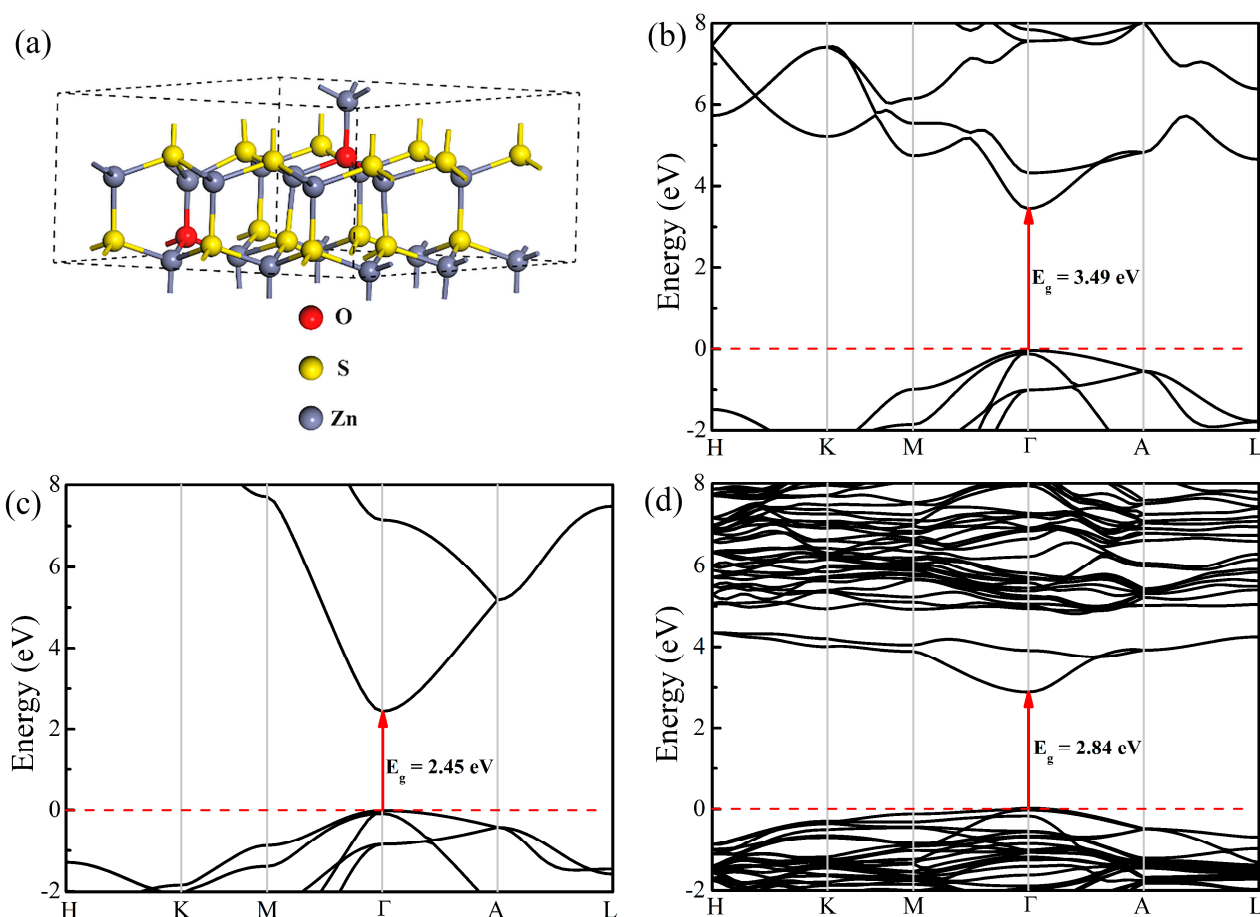


Figure 7. (a) Optimized atomic structure of ZnO/ZnS photocatalyst, Band structures near Fermi level for ZnS; (b), ZnO; (c) and ZnO/ZnS photocatalyst; (d) computed at HSE06 level (Fermi levels are set to zero).

Next, we investigated the electronic properties of ZnS, ZnO and ZnO/ZnS photocatalysts, and the energy band structures were shown in Figure 7b–d. The valence band maximum (VBM) and conduction band minimum (CBM) of the photocatalyst were all located at the Γ point, indicating that they were direct bandgap semiconductors with band gaps of 3.49, 2.45, and 2.84 eV, respectively.

To further investigate into the VBM and CBM compositions of the photocatalysts, the partial wave density of states (PDOS) was calculated and shown in Figure 8a–c. The VBMs of ZnS and ZnO were mainly derived from the p states of S and O atoms, and the 3p states of Zn atoms. For the ZnS/ZnO photocatalyst, the VBM and CBM mainly originated from the 3p states of S atoms and the 4s states of Zn atoms, indicating that a spatial separation of VBM and CBM occurred. To provide a more intuitive illustration, the spatial structures of the wave functions of the VBM and CBM for the ZnS/ZnO catalyst were calculated as shown in Figure 8d. The spatial separation of VBM and CBM can facilitate the efficient separation of photogenerated carriers. In addition, it can be seen that the band gap reduced when O atom was introduced into the ZnS system.

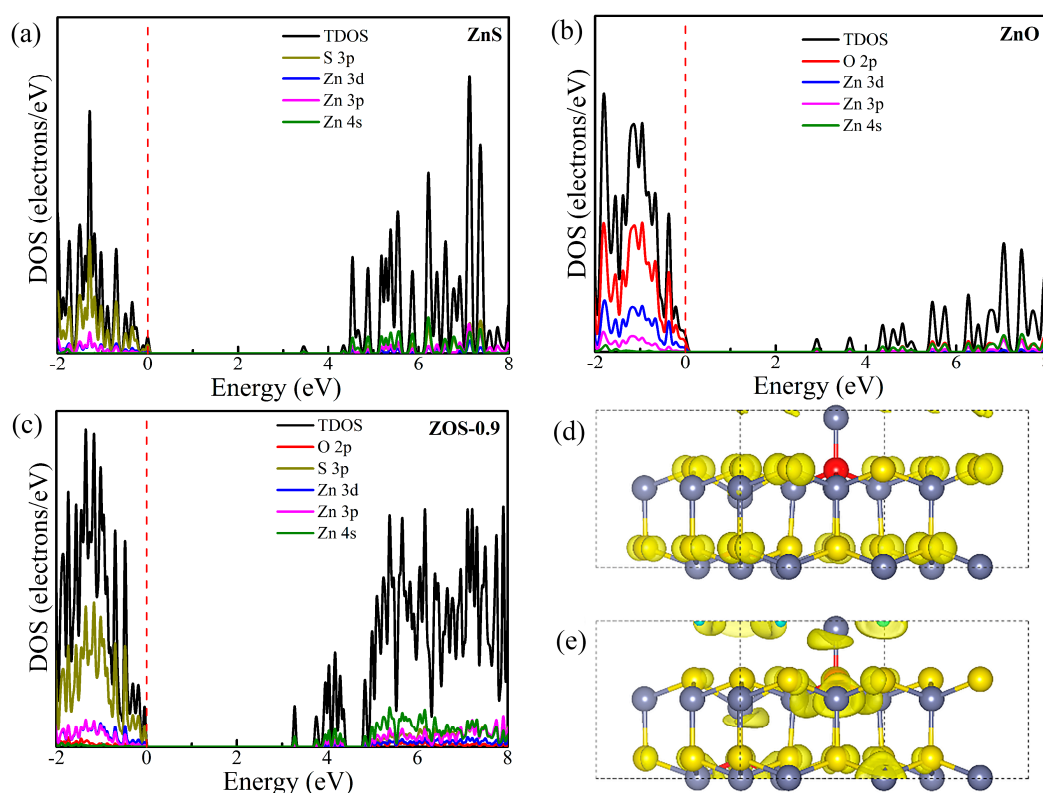


Figure 8. Partial density of states (PDOS) near Fermi level for ZnS (a), ZnO (b) and ZnO/ZnS photocatalyst (c), Spatial structure of wave functions of VBM (d) and CBM (e) for ZnS/ZnO photocatalyst.

2.3.2. Mechanism Characterization

The recombination speed of photogenerated carriers can be judged by the fluorescence emission spectrum. If the fluorescence intensity is high, it indicates that the photogenerated electron-hole recombination rate of the photocatalyst is fast. On the contrary, when the fluorescence intensity is low, it suggests that the recombination rate of photogenerated carriers is low. To further study the carrier separation characteristics of the samples, the fluorescence spectra of ZnO, ZnS and ZnO/ZnS photocatalysts were tested at an excitation wavelength of 250 nm and shown in Figure 9a. The fluorescence spectra intensities of ZnO and ZnS were higher, indicating that the electron-hole recombination probability was higher, and vice versa. While the fluorescence spectra intensities of ZnO/ZnS photocatalysts were obviously lower, and with the increase in ZnS content, the fluorescence intensity first decreased and then increased. When the molar ratio of ZnS and ZnO was 9:1, the fluorescence intensity of ZOS-0.9 was the lowest, indicating that the recombination possibility of photogenerated carriers was the lowest, so that more photogenerated electrons and holes can participate in the photocatalytic reaction, thereby improving the photocatalytic activity [48].

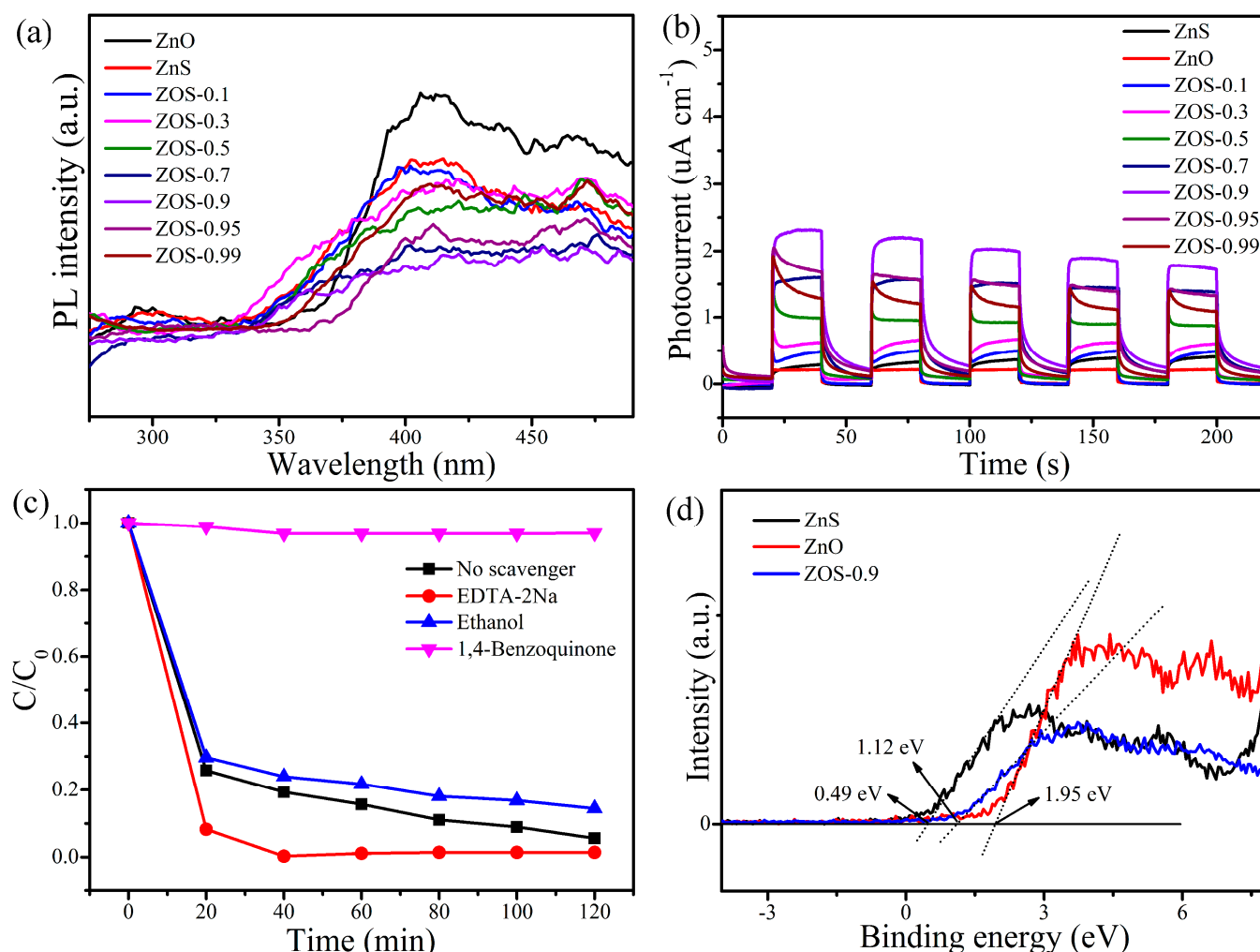


Figure 9. (a) Steady-state PL spectra of samples excited at 250 nm; (b) transient photocurrent responses of samples; (c) free radical capture experiment for degrading MO over ZnO/ZnS photocatalyst ZOS-0.9 under UV light; (d) XPS-VB spectra of ZnO, ZnS, and ZOS-0.9.

The photocurrent response characteristics were also investigated to reveal the photocatalytic mechanism of ZnO/ZnS. From Figure 9b, the photocurrent response signals of ZnO and ZnS were weaker while the photocurrent signal of ZnO/ZnS photocatalysts were stronger. The photocurrent signals also varied with the composition of ZnO/ZnS photocatalyst differing, when the molar ratio of ZnS and ZnO was 9:1, the ZOS-0.9 showed the highest photocurrent intensity, which was 10 times and 6 times than that of ZnO and ZnS, respectively, indicating that more photogenerated carriers can be produced over the ZnO/ZnS photocatalyst under illumination [49]. The ZnO/ZnS photocatalyst can effectively improve the migration rate of carriers and make it exhibit higher photocatalytic activity, which is consistent with the above photocatalytic results.

The active species in the photocatalytic reaction were studied via adding capture agents to the ZOS-0.9 system, in which EDTA-2Na, Ethanol, 1,4-Benzoquinone were the capture agents of h^+ , $\cdot\text{OH}$ and $\cdot\text{O}_2^-$, respectively. As shown in the Figure 9c, when EDTA-2Na was added to the reaction system under UV light irradiation, the catalytic activity was significantly improved, indicating that h^+ was not the active species for the reaction. When ethanol was added, the photocatalytic activity of ZOS-0.9 decreased, indicating the presence of $\cdot\text{OH}$, but it was not the main active species. However, when 1,4-Benzoquinone was added, the photocatalytic activity decreased significantly, indicating that $\cdot\text{O}_2^-$ was the major active species.

The valence band positions of ZnO, ZnS, and ZOS-0.9 were determined from the XPS valence band spectrum (XPS-VB). In Figure 9d, the valence band positions (E_{VB}) of ZnO, ZnS and ZOS-0.9 are 1.94, 0.49 and 1.12 eV, respectively. According to the formula $E_{CB} = E_{VB} - E_g$, the conduction band positions (E_{CB}) were -1.36 , -2.89 and -2.44 eV, respectively. From the above results, it can be seen that the photocatalyst ZOS-0.9 has strong oxidative and reductive abilities, attributing that the introduction of ZnO changed the energy band structure of the ZnO/ZnS photocatalyst and enhanced the redox ability.

2.3.3. Photocatalytic Mechanism

Based on the above photocurrent, fluorescence spectra, active species and XPS-VB results, it can be inferred that the ZnO/ZnS photocatalyst was a typical Type II photocatalytic mechanism (Figure 10).

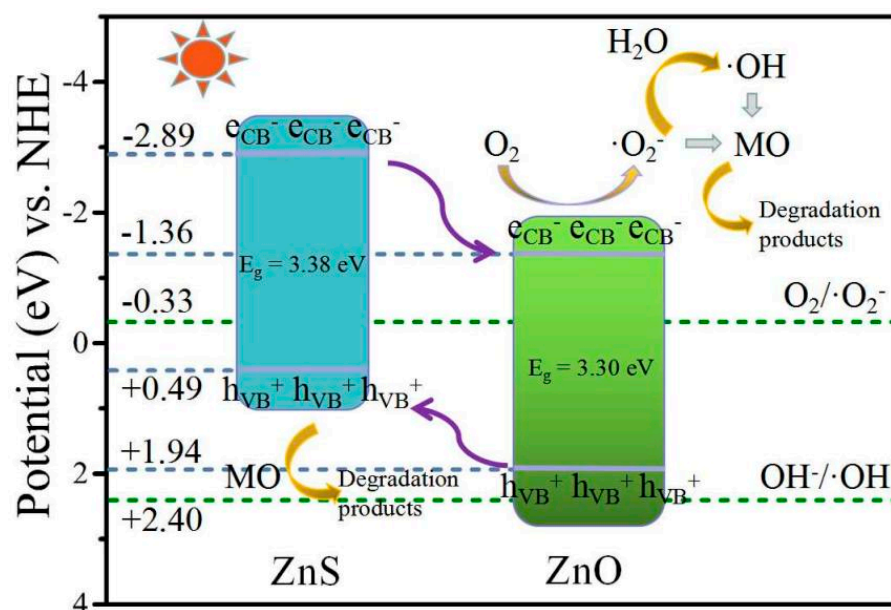


Figure 10. Photocatalytic mechanism of degradation MO over the ZnO/ZnS photocatalyst.

It can be found that ZnS and ZnO can both be excited by UV light to generate electrons in the conduction band and holes in the valence band, respectively. Among them, the electrons in the conduction band of ZnS can migrate to that of ZnO, while the holes in the valence band of ZnO can quickly migrate to the valence band of ZnS. In the above-mentioned electron and hole migration process, efficient separation of photogenerated carriers can be achieved, and effective time of photogenerated carriers can be improved. The photogenerated holes can directly catalyze and oxidize methyl orange, and then degrade it to CO_2 and H_2O . At the same time, the photogenerated electrons can combine with O_2 to generate $\cdot\text{O}_2^-$, and then react with pollutants to achieve the purpose of degradation.

3. Materials and Methods

3.1. Synthesis

ZnO/ZnS heterojunction photocatalysts were fabricated by a low-heat solid-state chemical process. Firstly, 10 mmol $\text{Zn}(\text{CH}_3\text{COO})_2 \cdot 2\text{H}_2\text{O}$ was added to a mortar and ground for 10 min, and 5 mmol sodium dodecyl sulfate (SDS) was added and ground for 40 min, then 1 mmol NH_2CSCH_3 was added and ground for 40 min, finally an excess of 40 mmol NaOH was added and continually ground for 60 min. The as-prepared sample was washed with deionized water and absolute ethanol, and dried in an oven at 80°C for 8 h to get ZnO/ZnS photocatalyst ZOS-0.1. Here, 0.1 represents that the molar ratio of ZnS to ZnO was 1:9.

For convenience, when the molar amounts of $\text{NH}_2\text{C}_5\text{CH}_3$ were 3 mmol, 5 mmol, 7 mmol, 9 mmol and 9.5 mmol, respectively, the ZnO/ZnS photocatalyst with different molar ratios was prepared according to a similar method, and were named as ZOS-0.3, ZOS-0.5, ZOS-0.7, ZOS-0.9 and ZOS-0.95, respectively. ZnS was obtained when NaOH and SDS were not added, and ZnO was got when NH_2CSCH_3 and SDS were absent.

3.2. Characterization

The crystal structures of samples were analyzed by X-ray powder diffractometer (D8 Advance, Bruker, Germany). The morphologies were characterized by field emission transmission electron microscopy (JEOL, JEM-2100F, Japan). The compositions of samples were tested by X-ray photoelectron spectroscopy (XPS) (SCIENTIFIC ESCALAB 250Xi, Thermo Company, Waltham, MA, USA). The ultraviolet-visible diffuse reflectance absorption spectra (UV-vis DRS) of the samples was measured by an ultraviolet-visible spectrometer (H-3900, Hitachi, Japan). The BaSO_4 tablet was used as a reference, and the scanning range was 250–800 nm. The fluorescence spectra of the samples were tested by a fluorescence spectrometer (F-4500, Hitachi, Japan), and the excitation wavelength of the sample was 250 nm. The photocurrent of the samples was measured using a CHI 660B electrochemical workstation. Here, three electrodes system including Ag/AgCl electrode, Pt sheet, and FTO glass coated with different samples were used as reference electrode, counter electrode, and working electrode, respectively.

3.3. Photocatalytic Test

The photocatalytic properties of the samples were carried out on a multi-tube photochemical reactor (Nanjing Xujiang Mechanical and Electrical Power Plant, XPA-7, China). During the experiment, the light source was a 300 W mercury lamp. Due to the high energy of the light source, more heat will be generated, so it is necessary to continuously introduce condensed water for circulating cooling. The specific operation is as follows: 25 mg catalyst was added to 50 mL of methyl orange (MO, 10 mg L^{-1}), rhodamine B (RhB, 10 mg L^{-1}) and tetracycline (10 mg L^{-1}) solution. In order to make the adsorption equilibrium between the catalyst and MO (RhB and tetracycline) solution, the adsorption was allowed to stand for 2 h under darkroom conditions. Subsequently, the light source was turned on to conduct the experiment. Under different light conditions, 3.5 mL of the reaction solution was taken at 20 min intervals, centrifuged at a certain speed ($10,000 \text{ r min}^{-1}$) for 10 min, the supernatant was taken and the concentrations of MO (RhB and tetracycline) were analyzed. The concentrations of MO (RhB and tetracycline) were measured using UV-Vis diffuse reflectance absorption spectrometer.

To investigate the active species in the photocatalytic reaction, radical trapping experiments were carried out. The scavengers used were mainly EDTA-2Na, Ethanol and 1,4-benzoquinone. The experimental procedure is the same as above, the photocatalyst and MO (RhB and tetracycline) concentrations remain unchanged, the difference is that a certain amount of trapping agent needs to be added to the above system.

3.4. Theoretical Calculation

First-principle calculations based on density functional theory (DFT) were carried out in the Vienna Ab initio Software Package (VASP) using plane-wave techniques [50]. The ion-electron interaction was described using the projected extended wave (PAW) method [51]. The function of Perdew, Burke and Ernzerhof (PBE) was used to describe the exchange-related energy [52]. A cut-off voltage of 450 eV was used for the plane wave base set. The first Brillouin zone was sampled using a Monkhorst-Pack k-point grid with K-point spacing less than 0.03 \AA^{-1} . The DFT-D3 method with Becke-Jonson damping is used to accurately explain for Van der Waals forces in weak interactions [53,54]. Considering that the PBE function systematically reduces the band gap, the band structure and density of states (DOS) were calculated using the Heyd-Scuseria-Ernzerh (HSE06) with mixed functions [55].

4. Conclusions

ZnO/ZnS photocatalysts were successfully prepared by a low-thermal solid-state chemical approach, and XRD, HRTEM and XPS results indicated that a ZnO/ZnS composite was formed, which could accelerate the efficient separation of photogenerated charges. The photocatalytic results showed that when the molar ratio of ZnS to ZnO was 9:1, the degradation rate of MO by ZOS-0.9 reached 95% after 120 min of irradiation under UV light, which was 12 times and 11 times than that of ZnO and ZnS, respectively. In addition, for the photocatalytic degradation of RhB and tetracycline, ZOS-0.7 exhibited excellent photocatalytic activity when the molar ratio of ZnS to ZnO was 7:3, indicating that the composite exhibited efficient and broad-spectrum photocatalytic performance. Based on the UV-Vis diffuse reflection absorption spectrum, fluorescence spectrum and surface photocurrent results, the excellent photocatalytic performance of ZnO/ZnS photocatalyst was mainly due to the enhancement of light absorption ability and the effective separation of carriers, mainly attributing to the interfacial effect of the ZnO and ZnS composite. The radical trapping results showed that the main active species for the degradation of MO in the ZnO/ZnS photocatalyst was $\cdot\text{O}_2^-$, combining with the theoretical calculation results, the photocatalytic mechanism belonged to type II. The study provides technical guidance for designing highly active ZnS composite photocatalysts.

Supplementary Materials: The following supporting information can be downloaded at: <https://www.mdpi.com/article/10.3390/catal12090981/s1>, Figure S1: Cycling experiment of photocatalytic degradation of MO by composite ZOS-0.9 under UV light irradiation.

Author Contributions: Conceptualization, X.J. and J.C.; methodology, F.C.; software, H.D.; validation, X.J. and J.C.; formal analysis, Z.W.; investigation, J.L.; resources, H.D.; data curation, F.C.; writing—original draft preparation, X.J.; writing—review & editing, J.C. and F.C.; visualization, H.D. and Z.W.; supervision, J.L. All authors have read and agreed to the published version of the manuscript.

Funding: The work was supported by Natural Science Foundation of Xinjiang Uygur Autonomous Region (No. 2021D01C034), Autonomous Region Key R&D Projects (No. 2022B01001), National Natural Science Foundation of China (No. 21666036, and 11764040), Tianshan Innovation Team Program of Xinjiang Uygur Autonomous Region (No. 2020D14038).

Conflicts of Interest: The authors declare no conflict of interest.

References

1. Lu, Y.; Zhang, H.; Fan, D.Q.; Chen, Z.P.; Yang, X.F. Coupling solar-driven photothermal effect into photocatalysis for sustainable water treatment. *J. Hazard. Mater.* **2022**, *423*, 127128. [CrossRef]
2. Nguyen, V.Q.; Mahadadalkar, M.A.; Rabie, A.M.; Shim, J.J. Microwave-assisted synthesis of a Z-scheme heterojunction Ag/AgBr@BiOBr/Bi₂O₃ photocatalyst for efficient organic pollutant degradation under visible light. *Environ. Sci. Nano* **2022**, *9*, 1724–1737. [CrossRef]
3. Liu, Y.; Zhang, Y.C.; Xu, X.F. Hydrothermal synthesis and photocatalytic activity of CdO₂ nanocrystals. *J. Hazard. Mater.* **2009**, *163*, 1310–1314. [CrossRef]
4. Choi, J.; Kim, H.H.; Lee, K.M.; Chen, N.; Kim, M.S.; Seo, J.; Lee, D.; Cho, H.; Kim, H.; Lee, J.; et al. Bicarbonate-enhanced generation of hydroxyl radical by visible light-induced photocatalysis of H₂O₂ over WO₃: Alteration of electron transfer mechanism. *Chem. Eng. J.* **2022**, *432*, 134401. [CrossRef]
5. Li, Y.; Zhao, Y.; Wu, J.; Han, Y.D.; Huang, H.; Liu, Y.; Kang, Z.H. Photo-charge regulation of metal-free photocatalyst by carbon dots for efficient and stable hydrogen peroxide production. *J. Mater. Chem. A* **2021**, *9*, 25453–25462. [CrossRef]
6. Zhang, F.; Zhang, Y.C.; Zhang, G.S.; Yang, Z.J.; Dionysiou, D.D.; Zhu, A.P. Exceptional synergistic enhancement of the photocatalytic activity of SnS₂ by coupling with polyaniline and N-doped reduced graphene oxide. *Appl. Catal. B Environ.* **2018**, *236*, 53–63. [CrossRef]
7. Zhao, X.Y.; Wang, X.; Zhao, Y.N.; Sun, H.Y.; Tan, H.Q.; Qiu, T.Y.; Zhao, Z.; Zhao, X.; Cheng, S.H.; Li, Y.G. Polyoxometalates-doped TiO₂/Ag hybrid heterojunction: Removal of multiple pollutants and mechanism investigation. *Environ. Sci. Nano* **2021**, *8*, 3855–3864. [CrossRef]
8. Li, K.; Ye, Y.; Zhang, W.C.; Hu, Y.Z.; Yang, Y.; Zhou, Y.; Liu, C. Modulation of the optical properties of ZnS QD-embedded glass through aluminum and manganese doping. *J. Mater. Chem. C* **2021**, *9*, 11261–11271. [CrossRef]
9. Zhan, W.Q.; Yuan, Y.; Yang, B.Q.; Jia, F.F.; Song, S.X. Construction of MoS₂ nano-heterojunction via ZnS doping for enhancing in-situ photocatalytic reduction of gold thiosulfate complex. *Chem. Eng. J.* **2020**, *394*, 124866. [CrossRef]

10. Rao, V.N.; Ravi, P.; Sathish, M.; Reddy, N.L.; Lee, K.; Sakar, M.; Prathap, P.; Kumari, M.M.; Reddy, K.R.; Nadagouda, M.N.; et al. Monodispersed core/shell nanospheres of ZnS/NiO with enhanced H₂ generation and quantum efficiency at versatile photocatalytic conditions. *J. Hazard. Mater.* **2021**, *413*, 125359.
11. Shukla, R.S.; Zala, V.B.; Gupta, S.K.; Gajjar, P.N. ZnS/CdX (X = S, Se, Te) core/shell nanowires: An attempt at tuning the electronic bandgaps and SQ Efficiencies. *J. Mater. Chem. C* **2021**, *9*, 6605–6617. [[CrossRef](#)]
12. Gao, T.T.; Lu, C.; Lyu, L. H₂O₂ inducing dissolved oxygen activation and electron donation of pollutants over Fe-ZnS quantum dots through surface electron-poor/rich microregion construction for water treatment. *J. Hazard. Mater.* **2021**, *420*, 126579. [[CrossRef](#)]
13. Amani-Ghadim, A.R.; Khodam, F.; Dorraji, M.S.S. ZnS quantum dot intercalated layered double hydroxide semiconductors for solar water splitting and organic pollutant degradation. *J. Mater. Chem. A* **2019**, *7*, 11408–11422. [[CrossRef](#)]
14. Chen, S.H.; Xiao, X.Y.; Li, P.H.; Li, Y.X.; Yang, M.; Guo, Z.; Huang, X.J. A direct Z-scheme ZnS/Co₉S₈ heterojunction based photoelectrochemical sensor for the highly sensitive and selective detection of chlorpyrifos. *Environ. Sci. Nano* **2020**, *7*, 753–763. [[CrossRef](#)]
15. Serrà, A.; Philippe, L. Simple and scalable fabrication of hairy ZnO@ZnS core@shell Cu cables for continuous sunlight-driven photocatalytic water remediation. *Chem. Eng. J.* **2020**, *401*, 126164. [[CrossRef](#)]
16. Fatima, H.; Azhar, M.R.; Zhong, Y.J.; Arafat, Y.; Khiadani, M.; Shao, Z.P. Rational design of ZnO-zeolite imidazole hybrid nanoparticles with reduced charge recombination for enhanced photocatalysis. *J. Colloid Interf. Sci.* **2022**, *614*, 538–546. [[CrossRef](#)]
17. Rong, P.; Jiang, Y.F.; Wang, Q.; Gu, M.; Jiang, X.L.; Yu, Q. Photocatalytic degradation of methylene blue (MB) with Cu₁-ZnO single atom catalysts on graphene-coated flexible substrates. *J. Mater. Chem. A* **2022**, *10*, 6231–6241. [[CrossRef](#)]
18. Chinnathambi, A. Synthesis and characterization of spinel FeV₂O₄ coupled ZnO nanoplates for boosted white light photocatalysis and antibacterial applications. *J. Alloys Compd.* **2021**, *890*, 161742. [[CrossRef](#)]
19. Guo, X.Y.; Liu, S.; Wang, W.J.; Li, C.Y.; Yang, Y.; Tian, Q.H.; Liu, Y. Plasmon-induced ultrafast charge transfer in single-particulate Cu_{1.94}S-ZnS nanoheterostructures. *Nanoscale Adv.* **2021**, *3*, 3481–3490. [[CrossRef](#)]
20. Wang, X.W.; Cao, Z.Q.; Zhang, Y.; Xu, H.P.; Cao, S.S.; Zhang, R.B. All-solid-state Z-scheme Pt/ZnS-ZnO heterostructure sheets for photocatalytic simultaneous evolution of H₂ and O₂. *Chem. Eng. J.* **2020**, *385*, 123782. [[CrossRef](#)]
21. Giroux, M.S.; Zahra, Z.; Salawu, O.A.; Burgess, R.M.; Ho, K.T.; Adeleye, A.S. Assessing the environmental effects related to quantum dot structure, function, synthesis and exposure. *Environ. Sci. Nano* **2022**, *9*, 867–910. [[CrossRef](#)]
22. Jing, M.J.; Chen, Z.G.; Li, Z.; Li, F.Y.; Chen, M.J.; Zhou, M.J.; He, B.H.; Chen, L.; Hou, Z.H.; Chen, X.B. Facile Synthesis of ZnS/N,S Co-doped Carbon Composite from Zinc Metal Complex for High-Performance Sodium-Ion Batteries. *ACS Appl. Mater. Interfaces* **2018**, *10*, 704–712. [[CrossRef](#)]
23. Li, H.B.; Sun, T.Q.; Zhang, L.X.; Cao, Y.A. Matching and adjusting energy band structures of Pd-modified sulphides (ZnS, In₂S₃ and CuS) and improving the photocatalytic activity of CO₂ photoreduction. *Nanoscale* **2020**, *12*, 18180–18192. [[CrossRef](#)]
24. Gao, F.; Yuan, J.; Huang, X.Y.; Lei, R.; Jiang, C.K.; Zhuang, J.D.; Liu, P. Directional transfer of photo-generated charges mediated by cascaded dual defects in ternary photocatalyst ZnS/ZnO-In₂O₃ with enhanced photocatalytic performance. *Chem. Eng. J.* **2021**, *416*, 129159. [[CrossRef](#)]
25. Jin, X.K.; Chen, F.J.; Jia, D.Z.; Cao, Y.L.; Duan, H.M.; Long, M.Q.; Yang, L.Y. Influences of synthetic conditions on the photocatalytic performance of ZnS/graphene composites. *J. Alloys Compd.* **2019**, *780*, 299–305. [[CrossRef](#)]
26. Liu, B.L.; Li, Y.Z.; Wang, K.; Cao, Y.L. The solid-state in situ construction of Cu₂O/CuO heterostructures with adjustable phase compositions to promote CO oxidation activity. *CrystEngComm* **2020**, *22*, 7808–7815. [[CrossRef](#)]
27. Wang, R.Y.; Jia, D.Z.; Cao, Y.L. Facile synthesis and enhanced electrocatalytic activities of organic-inorganic hybrid ionic liquid polyoxometalate nanomaterials by solid-state chemical reaction. *Electrochim. Acta* **2012**, *72*, 101–107. [[CrossRef](#)]
28. Chen, F.J.; Cao, Y.L.; Jia, D.Z. A room-temperature solid-state route for the synthesis of graphene oxide-metal sulfide composites with excellent photocatalytic activity. *CrystEngComm* **2013**, *15*, 4747–4754. [[CrossRef](#)]
29. Chen, F.J.; Jin, X.K.; Cao, Y.L.; Jia, D.Z.; Liu, A.J.; Wu, R.; Long, M.Q. Effects of the synthesis conditions on the photocatalytic activities of sulfide-graphene oxide composites. *Dyes Pigments* **2019**, *163*, 177–188. [[CrossRef](#)]
30. Li, Y.Z.; Cao, Y.L.; Jia, D.Z. A general strategy for synthesis of metal nanoparticles by a solid-state redox route under ambient conditions. *J. Mater. Chem. A* **2014**, *2*, 3761–3765. [[CrossRef](#)]
31. Du, X.J.; Hu, J.D.; Xie, J.; Hao, A.Z.; Lu, Z.J.; Cao, Y.L. Simultaneously tailor band structure and accelerate charge separation by constructing novel In(OH)₃-TiO₂ heterojunction for enhanced photocatalytic water reduction. *Appl. Surf. Sci.* **2022**, *593*, 153305. [[CrossRef](#)]
32. Chen, F.J.; Jin, X.K.; Jia, D.Z.; Cao, Y.L.; Duan, H.M.; Long, M.Q. Efficient treatment of organic pollutants over CdS/graphene composites photocatalysts. *Appl. Surf. Sci.* **2020**, *504*, 144422. [[CrossRef](#)]
33. Liu, B.L.; Cao, Y.L.; Zhang, H.Y.; Wang, S.Q.; Geng, Q.; Li, Y.Z. Constructing ultrafine Cu nanoparticles encapsulated by N-doped carbon nanosheets with fast kinetics for high-performance lithium/sodium storage. *Chem. Eng. J.* **2022**, *446*, 136918. [[CrossRef](#)]
34. Zhou, M.; Ying, Y.; Huang, H.; Tan, Y.M.; Deng, W.F.; Xie, Q.J. Photoelectrochemical immunoassay of interleukin-6 based on covalent reaction-triggered photocurrent polarity switching of ZnO@fullerenol. *Chem. Commun.* **2021**, *57*, 10903–10906. [[CrossRef](#)]
35. Zhang, K.; Zhuo, Z.H.; Fan, G.R.; Wang, Z.D.; Chen, S.X.; Xu, L.L.; Wen, Y.P.; Wang, P. Nano-ZnS decorated hierarchically porous carbon electrocatalyst with multiple enzyme-like activities as a nanozyme sensing platform for simultaneous detection of dopamine, uric acid, guanine, and adenine. *Nanoscale* **2021**, *13*, 20078–20090. [[CrossRef](#)]

36. Dadigala, R.; Bandi, R.; Gangapuram, B.R.; Guttena, V. Construction of in situ self-assembled FeWO₄/g-C₃N₄ nanosheet heterostructured Z-scheme photocatalysts for enhanced photocatalytic degradation of rhodamine B and tetracycline. *Nanoscale Adv.* **2019**, *1*, 322–333. [[CrossRef](#)]
37. Su, T.M.; Hood, Z.D.; Naguib, M.; Bai, L.; Luo, S.; Rouleau, C.M.; Ivanov, I.N.; Ji, H.B.; Qin, Z.Z.; Wu, Z.L. 2D/2D heterojunction of Ti₃C₂/g-C₃N₄ nanosheets for enhanced photocatalytic hydrogen evolution. *Nanoscale* **2019**, *11*, 8138–8149. [[CrossRef](#)]
38. Li, Z.H.; Pan, X.Y.; Yi, Z.G. Photocatalytic oxidation of methane over CuO decorated ZnO nanocatalysts. *J. Mater. Chem. A* **2019**, *7*, 469–475. [[CrossRef](#)]
39. Xiong, J.H.; Li, Y.L.; Lu, S.J.; Guo, W.; Zou, J.H.; Fang, Z.B. Controllable sulphur vacancies confined in nanoporous ZnS nanoplates for visible-light photocatalytic hydrogen evolution. *Chem. Commun.* **2021**, *57*, 8186–8189. [[CrossRef](#)]
40. Wu, Q.H.; Abdeta, A.B.; Kuo, D.H.; Zhang, H.Y.; Lu, Q.X.; Zhang, J.B.; Zelekew, O.A.; Mosisa, M.T.; Lin, J.G.; Chen, X.Y. A molybdenum sulfo-oxide/cobalt oxysulfide Z scheme heterojunction catalyst for efficient photocatalytic hydrogen production and pollutant reduction. *J. Mater. Chem. A* **2022**, *10*, 5328–5349. [[CrossRef](#)]
41. Ma, X.Y.; Gao, Y.F.; Yang, B.; Lou, X.J.; Huang, J.B.; Ma, L.J.; Jing, D.W. Enhanced charge separation in La₂NiO₄ nanoplates by coupled piezocatalysis and photocatalysis for efficient H₂ evolution. *Nanoscale* **2022**, *14*, 7083–7095. [[CrossRef](#)] [[PubMed](#)]
42. Zhu, Z.Y.; Li, J.Y.; Li, W.; Liu, X.Y.; Dang, Y.Y.; Ma, T.H.; Wang, C.Y. Simulated-sunlight-driven Cr(VI) reduction on a type-II heterostructured Sb₂S₃/CdS photocatalyst. *Environ. Sci. Nano* **2022**, *9*, 1738–1747. [[CrossRef](#)]
43. Mai, H.X.; Chen, D.H.; Tachibana, Y.; Suzuki, H.; Ab, R.; Caruso, R.A. Developing sustainable, high-performance perovskites in photocatalysis: Design strategies and applications. *Chem. Soc. Rev.* **2021**, *50*, 13692–13729. [[CrossRef](#)]
44. Gao, X.X.; Wang, J.; Yu, J.L.; Xu, H.B. Novel ZnO–ZnS nanowire arrays with heterostructures and enhanced photocatalytic properties. *CrystEngComm* **2015**, *17*, 6328–6337. [[CrossRef](#)]
45. Bano, K.; Mittal, S.K.; Singh, P.P.; Kaushal, S. Sunlight driven photocatalytic degradation of organic pollutants using a MnV₂O₆/BiVO₄ heterojunction: Mechanistic perception and degradation pathways. *Nanoscale Adv.* **2021**, *3*, 6446–6458. [[CrossRef](#)]
46. Zhou, Q.L.; Li, L.; Xin, Z.C.; Yu, Y.; Wang, L.X.; Zhang, W.Z. Visible light response and heterostructure of composite CdS@ZnS–ZnO to enhance its photocatalytic activity. *J. Alloys Compd.* **2020**, *813*, 152190. [[CrossRef](#)]
47. Deng, F.; Zhao, L.N.; Luo, X.B.; Luo, S.L.; Dionysiou, D.D. Highly efficient visible-light photocatalytic performance of Ag/AgIn₅S₈ for degradation of tetracycline hydrochloride and treatment of real pharmaceutical industry wastewater. *Chem. Eng. J.* **2018**, *333*, 423–433. [[CrossRef](#)]
48. Wang, Y.; Zhao, X.; Wang, L.; Yang, Y.; Jiao, L.; Wu, Z.H.; Gao, X.; Cheng, S.; Lin, M.Z. A novel nano-sized red phosphorus decorated borocarbonitride heterojunction with enhanced photocatalytic performance for tetracycline degradation. *Environ. Sci. Nano* **2022**, *9*, 1869–1878. [[CrossRef](#)]
49. Zhang, F.; Zhang, Y.C.; Wang, Y.Y.; Zhu, A.P.; Zhang, Y. Efficient photocatalytic reduction of aqueous Cr(VI) by Zr⁴⁺ doped and polyaniline coupled SnS₂ nanoflakes. *Sep. Purif. Technol.* **2022**, *283*, 120161. [[CrossRef](#)]
50. Kresse, G.; Furthmüller, J. Efficient iterative schemes for ab initio total-energy calculations using a plane-wave basis set. *Phys. Review B* **1996**, *54*, 11169–11186. [[CrossRef](#)]
51. Kresse, G.; Joubert, D. From ultrasoft pseudopotentials to the projector augmented-wave method. *Phys. Rev. B* **1999**, *59*, 1758–1775. [[CrossRef](#)]
52. Perdew, J.P.; Burke, K.; Ernzerhof, M. Generalized gradient approximation made simple. *Phys. Rev. Lett.* **1996**, *77*, 3865–3868. [[CrossRef](#)] [[PubMed](#)]
53. Grimme, S.; Antony, J.; Ehrlich, S.; Krieg, H. A consistent and accurate ab initio parametrization of density functional dispersion correction (DFT-D) for the 94 elements H–Pu. *J. Chem. Phys.* **2010**, *132*, 154104–154119. [[CrossRef](#)]
54. Grimme, S.; Ehrlich, S.; Goerigk, L. Effect of the damping function in dispersion corrected density functional theory. *J. Comput. Chem.* **2010**, *32*, 1456–1465. [[CrossRef](#)]
55. Heyd, J.; Scuseria, G.E.; Ernzerhof, M. Hybrid functionals based on a screened Coulomb potential. *J. Chem. Phys.* **2003**, *118*, 8207–8215. [[CrossRef](#)]